Accurate Modeling of High-Q Spiral Inductors in Thin-Film Multilayer Technology for Wireless Telecommunication Applications

Philip Pieters, *Student Member, IEEE*, Kristof Vaesen, Steven Brebels, *Student Member, IEEE*, Samir F. Mahmoud, *Senior Member, IEEE*, Walter De Raedt, Eric Beyne, and Robert P. Mertens, *Fellow, IEEE*

***Abstract*—In the current trend toward portable applications, high-Q integrated inductors are gaining a lot of importance. Using thin-film multilayer or multichip-module-deposition technology, high-Q circular inductors for RF and microwave applications may be integrated efficiently. Their quality factors may go up to over 100. In this paper, an accurate analytical model for such multiturn circular spiral inductors embedded in a thin-film multilayer topology is presented. Starting from the geometrical parameters, the model provides an accurate prediction of the inductance value, Q factor and frequency behavior of the inductor. This allows a "first-time-right"' realization of the integrated component and provides opportunities for fast optimization of the inductors. Finally, the presented high-Q inductors have been used in various integrated RF and microwave subsystems for wireless applications, of which a number are discussed at the end of this paper.**

***Index Terms*—Coplanar, high-Q, MCM-D, spiral inductor, thin-film multilayer, wireless.**

I. Introduction

TELECOMMUNICATIONS systems, e.g., front-ends for wireless applications, use a considerable amount of passive components. In conventional microwave integrated circuits (MICs), these passives are surface-mounted devices, consuming a large area and yielding a high mounting cost. Therefore, miniaturization and integration or embedding of the passive components has become a major task [1], [2]. This is especially the case for high-quality inductors, which are required for low-power, low-noise, and high-bandwidth portable applications [3], [4].

A possible miniaturization route is integrating the passive components together with the active device on radio-frequency integrated circuits (RFICs). This has the disadvantage that, e.g., passive components such as spiral inductors will consume the major part of the expensive silicon area. Moreover, in standard processing, the silicon substrate losses limit the quality (Q) factor of these inductors to about eight, which impedes using these components in high-performance and high-frequency applications. By applying special nonstandard materials and techniques, such thicker aluminum [5], multilevel interconnects [6], copper–damascene interconnects, high-resistivity silicon or sapphire substrates, or special solenoidal and three-dimensional designs [7]–[9], the Q factor of the inductors on silicon may be increased up to about 20 to 25 at the expense of a large increase of cost.

Looking for alternative solutions, thin-film multilayer technologies, such as multichip module deposition (MCM-D) technology, are gaining more and more interest as an excellent enabling technology to fulfill the current miniaturization objectives. MCM-D technology was originally used for the interconnection of high-speed digital chips within a single package [10]–[14]. However, recent developments have demonstrated that because of its excellent dimension control and the use of high-quality materials, this technology may be used for high-frequency analog applications. Integrated passive components [15]–[19], couplers [20], [21], baluns [21], [22], and even antennas at microwave frequencies [23]–[25] have been demonstrated in MCM-D. Furthermore, the first complete MCM-D RF subsystem demonstrator modules are also being developed [26], [27]. The advantage of MCM-D technology is that copper metallization may be combined with very low-loss dielectric materials at a low cost in a thin-film integrated circuit (IC)-like manufacturing process. In this way, both resistive losses, as well as dielectric losses, may be kept very low [28], boosting its applicability for high frequencies and high-quality passive structures. This is especially beneficial for integrated spiral inductors. Moreover, the MCM-D substrate with integrated passives may act as a carrier and interconnection medium for active circuits mounted by wire bonding or flip chip [26], [27]. This allows optimization of the complete RF systems in terms of chip-package co-design [29].

In this paper, a thin-film multilayer MCM-D technology for microwave integrated passive components is presented. More specifically, we will focus on the design, modeling, and realization of integrated spiral inductors with very high-Q factors up to more than 100 at microwave frequencies. In Section VII, a number of RF and microwave subsystems for wireless applications using these high-Q spiral inductors are briefly presented.

Manuscript received April 25, 2000. This work was supported by the European Space Agency under Contract 13627/99/NL/FM (SC) and by the National Semiconductor Corporation. The work of S. Brebels was supported by the Flemish Institute for Promotion of Scientific Technological Research in Industry.

P. Pieters is with the Engineering and Technology Development Department, CS2, B-1930 Zaventem, Belgium.

K. Vaesen, S. Brebels, W. De Raedt, and E. Beyne are with the Materials and Components Packaging Division, Interuniversity Microelectronics Centre, B-3001 Leuven, Belgium.

S. F. Mahmoud is with the Electrical and Computer Engineering Department, Kuwait University, Safat 13060, Kuwait.

R. P. Mertens is with the Interuniversity Microelectronics Centre, B-3001 Leuven, Belgium and is also with the Catholic University of Leuven, B-3001 Leuven, Belgium.

Publisher Item Identifier S 0018-9480(01)02421-8.

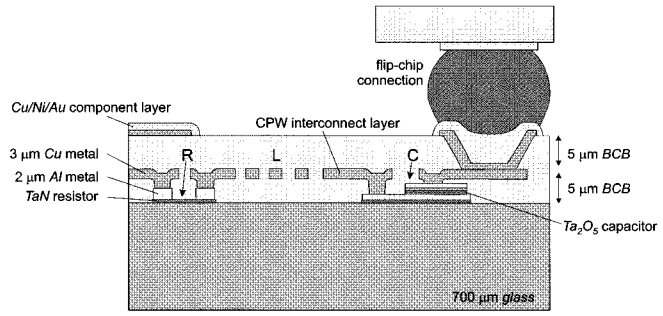

Fig. 1. Basic buildup structure of the thin-film multilayer MCM-D technology for the integration of passive components used in this study.

II. Thin-Film Multilayer MCM-D Technology for Integrated Passive Components

In Fig. 1, a cross section of the thin-film multilayer buildup used in this study is shown. The different sputtered metal layers are separated by thin spun-on layers of photosensitive benzocyclobutene (BCB) dielectric ($\varepsilon_r = 2.65$ and $\tan\delta = 8 \cdot 10^{-4}$) stacked on a low-loss borosilicate-based glass carrier substrate ($\varepsilon_r = 6.2$ and $\tan\delta = 9 \cdot 10^{-4}$). Immediately on the carrier substrate, TaN resistors (with $R_\square = 25\,\Omega$) and $\mathrm{Ta_2O_5}$ capacitors $(\varepsilon_r = 25)$ may be realized. These resistors and capacitors are contacted with an aluminum metallization, while the further interconnections and spiral inductors are realized using the other high-conductivity copper layers. Vias with a minimum diameter of 10 μm are used to connect the different metal layers. The top copper layer is coated with NiAu in order to allow easy mounting of other active devices (flip chip, wire bonding). The uncovered BCB at the air interface also serves as a passivation layer since it is very stable, very corrosion hard, and has a very low moisture absorption [30].

The spiral inductors are realized on the central 3-μm-thick coplanar interconnection layer. These are multiturn circular coils in a coplanar style, with total diameters ranging from 300 up to 3000 μm, inductance values from 0.5 nH up to about 80 nH, and an usable frequency range up to 20 GHz. The connection from the center of the coil to the outside is realized using the upper metallization. As will be discussed below, unloaded Q factors of over 100 have been achieved. Fig. 2 presents a photograph of a typical spiral inductor integrated in this technology.

III. Experimental Results

A whole series of circular spiral inductors with different linewidths, spaces, and number of turns has been realized in the thin-film multilayer MCM-D technology. On-wafer high-frequency vector-network analyzer measurements were performed using coplanar probes. A representative set of nine typical inductors with different conductor widths and number of turns is listed in Table I. For this set of spirals, the important characteristics of inductance value and Q factor versus frequency are displayed in Fig. 3. For small inductor values, L remains practically constant over the whole measured frequency range (i.e., the first self-resonance frequency lies much beyond this range). The larger L becomes, the earlier the nonconstant inductance behavior starts.

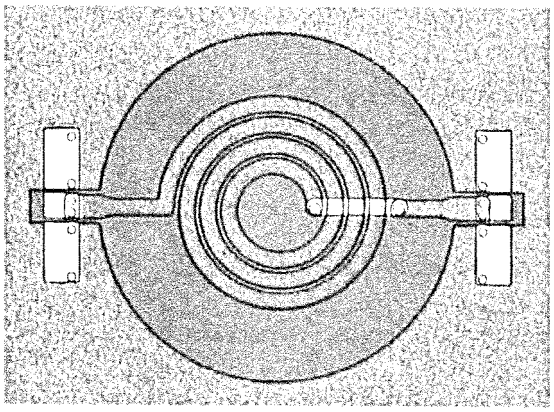

Fig. 2. Photograph of a typical integrated spiral inductor (3.5 turns, 50-μm-wide conductors with 20-μm spacing, the inner and outer gaps are 200 μm, the total diameter is 1185 μm).

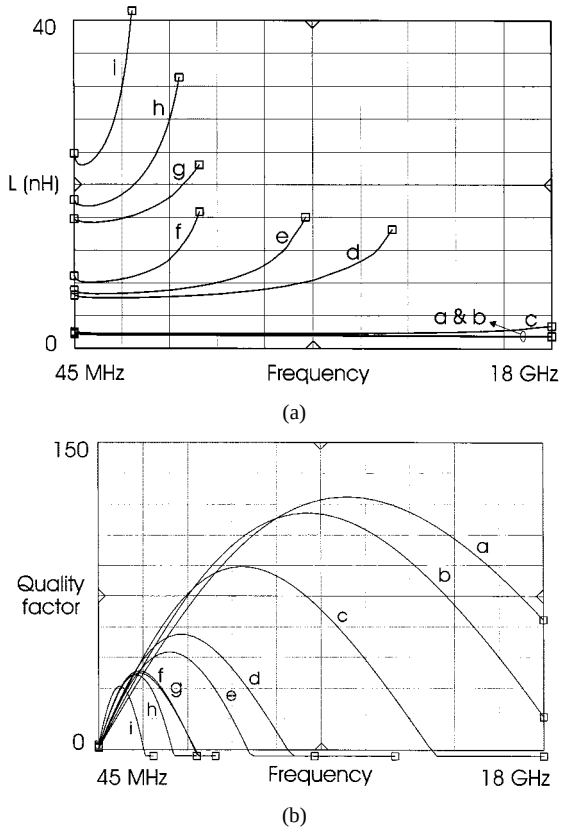

Fig. 3. (a) Measured inductance value versus frequency for a typical set of MCM-D inductors. The labels a–i refer to the spirals listed in Table I. The inductance curve for spirals a and b practically coincide in the displayed frequency range. (b) Measured inductor quality factor versus frequency for a typical set of MCM-D inductors. The labels a–i refer to the spirals listed in Table I, e.g., spiral a has a very high-Q factor of 123. The Q factor curve for spirals f and g practically coincide.

The Q factor is obtained from

$$Q = \frac{\mathrm{imag}(Z\mathrm{in})}{\mathrm{real}(Z\mathrm{in})} \tag{1}$$

using the inductor input impedance $Z\mathrm{in} = 1/Y11$. The unloaded Q values of the small inductors are clearly much higher than 100.

TABLE I
DIMENSIONS FOR NINE TYPICAL MCM-D SPIRAL INDUCTORS WITH DIFFERENT CONDUCTOR WIDTHS AND NUMBER OF TURNS. FOR ALL SPIRALS, THE CONDUCTOR SPACING IS KEPT 20 μm, THE INNER GAP 100 μm, AND SPACING TO THE COPLANAR GROUND PLANE 200 μm

Spiral label	a	b	c	d	e	f	g	h	i
Conductor width (μm)	30	50	100	30	50	100	30	50	100
Number of turns	1.5	1.5	1.5	3.5	3.5	3.5	5.5	5.5	5.5
Total outer diameter (μm)	380	460	660	580	740	1140	780	1020	1620

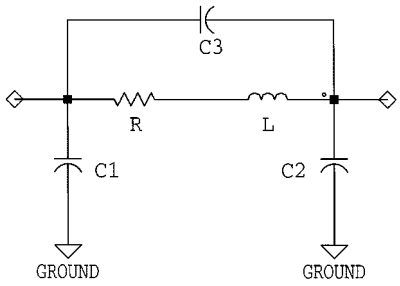

Fig. 4. First-order lumped equivalent spiral inductor model.

In Section IV, a new analytical model is developed in order to predict the frequency behavior of this type of spiral inductors, starting from the geometrical parameters.

IV. SPIRAL INDUCTOR MODEL

When having passive components integrated in a multilayer technology, trimming becomes very difficult, if not impossible. Therefore, accurate models are extremely important to have first-time-right values. In this section, an accurate analytical spiral inductor model predicting the behavior of the circular spiral inductors integrated in a coplanar topology in a thin-film multilayer buildup is discussed. Starting from geometrical parameters such as conductor width, spacing between the turns and number of turns, the inductance values, the losses, and the parasitic capacitances are calculated. This allows the determination of the Q factor and the frequency behavior of the inductor.

When using inductors, one is generally only interested in its behavior up to the first self-resonance frequency. Therefore, the single-section lumped-element model shown in Fig. 4 will characterize the component sufficiently enough. In this model, R accounts for the resistive losses, L includes the desired inductive effect, and the C's model the capacitive coupling effects (C_1 and C_2 are related to the capacitive coupling between the coil and surrounding ground plane, C_3 models the coupling in between the turns of the coil itself). Since low-loss dielectric materials are used, the substrate conductance typically put in shunt with the capacitances to ground may be omitted.

The following calculations will now provide the values of the elements in this lumped-element model starting from the geometry of the inductor and taking the thin-film multilayer buildup in to account.

A. Inductance

The calculation of the inductance values is based on [31]. The spiraling coils are approximated by concentric rings in the multilayer structure. For a single ring (lying in the horizontal plane $z = 0$) with width w and mean radius a, w is considered much smaller than a. We assume a harmonically time-varying electric surface-current density J A/m flowing in ring, with a radial current distribution $f(r) = (w/\pi)[(w/2)^2 - (r-a)^2]^{-1/2}$, which takes the edge effect into account. After determination of the electromagnetic fields associated with the current, and derivation of the magnetic flux linkage with the ring, the primary inductance L_p of the ring in free space becomes

$$L_p = \pi\mu_0 a^2 \int_0^\infty \frac{g}{u_0} J_1^2(ga) J_0\left(g\frac{a}{2}\right) \partial g \tag{2}$$

with g being the wavenumber (m^{-1}). Re-expression in dimensionless quantities by using the substitution $x = ga$ and $\bar{w} = w/(2a)$ and assuming that the ring radius is much smaller than the free-space wavelength, the quasi-static primary inductance of the ring may be written as

$$L_p = \pi\mu_0 a \int_0^\infty J_1^2(x) J_0(x\bar{w}) dx \tag{3}$$

with J_0 and J_1 being the zeroth- and first-order Bessel functions of the first kind and μ_0 the permeability of free space.

The effect of the multilayer is included considering the Fresnel reflection coefficient $\Gamma(g)$ of the cylindrical wavelet $J_0(gr)\ \exp(u_0 z)$ incident on the planar structure. In the presence of the lower half-space, the primary inductance of the ring finally becomes

$$L_p = \pi\mu_0 a \int_0^\infty J_1^2(x) J_0(x\bar{w})\{1 + \Gamma(x)\} dx. \tag{4}$$

Under the quasi-static approximation (dielectric losses negligible), the dielectric layers and carrier substrate layer appear to be transparent and the inductance is only affected by the ground plane. In this case, the Fresnel coefficient becomes

$$\Gamma(x) = -\exp\left[-2g(h_{\mathrm{BCB}} + h_{\mathrm{glass}})\right]. \tag{5}$$

Besides the primary self-inductance of the concentric rings, the mutual inductance M between these rings will also add to the total inductance of the spiral inductor. The formulation given above may be adapted to obtain the mutual inductance between two concentric rings with mean radii a and b (with $b < a$ and $w \ll a, b$ and $w \ll (b-a)$), assuming that the ring currents are concentrated at the mean radii of the rings. This means that w becomes zero, thus yielding

$$M(a,b) = \pi\mu_0 b \int_0^\infty J_1(x) J_1\left(x\frac{b}{a}\right) dx. \tag{6}$$

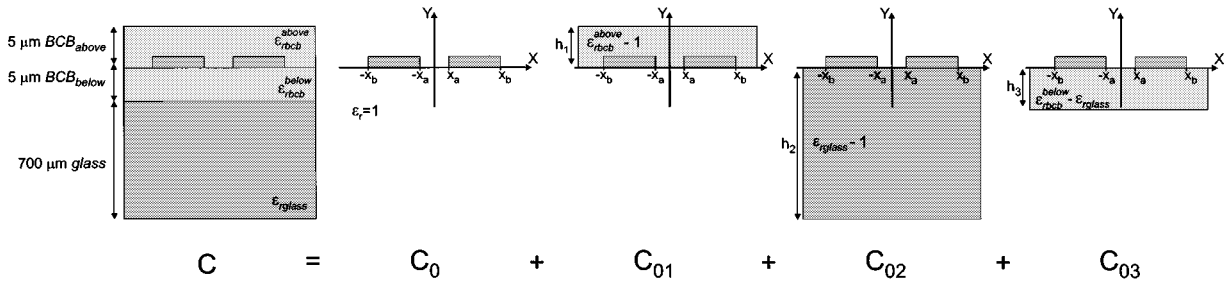

Fig. 5. Configuration used in the superposition of partial capacitance method for the determination of the effective relative permittivity between two metal strips embedded in a thin-film multilayer structure.

This equation may be expressed in terms of the complete elliptic integrals $K(\cdot)$ and $E(\cdot)$ as

$$M(a,b) = \pi\mu_0\sqrt{ab}\left(\frac{2}{\pi}\sqrt{\frac{a}{b}}\right)\left[K\left(\frac{b}{a}\right) - E\left(\frac{b}{a}\right)\right]. \quad (7)$$

Finally, the total inductance L of the multiturn spiral inductor is calculated as the sum of the self-inductances of each concentric ring according to (4), together with the sum of the mutual inductances between each couple of neighboring rings according to (7).

B. Capacitances

In order to calculate the capacitive coupling between equiplanar conductors embedded in a multilayer structure, the effective relative permittivity ε_{eff} of the structure has to be known. Using conformal mapping and superposition of partial capacitances, analytical formulas for the determination ε_{eff} in the quasi-static case may be derived [32]. With C_0 the capacitance between the metal strips in free space and C the actual capacitance between the strips on the multilayer structure, the basic equation

$$\varepsilon_{\text{eff}} = \frac{C}{C_0} \quad (8)$$

holds. Furthermore, the actual capacitance C may be written as the sum of four capacitances $C = C_0 + C_{01} + C_{02} + C_{03}$, as indicated in Fig. 5.

Using conformal mapping and Schwartz transformations, the capacitance C_0 in the absence of all dielectrics is given by

$$C_0 = \varepsilon_0\frac{K(k)}{K(k')} \quad (9)$$

where $k = \sqrt{1-(x_a/x_b)^2}$ and $k' = \sqrt{1-k^2}$.

Next, by applying a method similar to [32], the final equation for the effective relative permittivity between the coplanar strips becomes

$$\begin{aligned}\varepsilon_{\text{eff}} =& 1 + \frac{1}{2}\left(\varepsilon_{r\text{BCB}}^{\text{above}-1}\right)\frac{K(k)K(k_1')}{K(k')K(k_1)} \\ &+ \frac{1}{2}\left(\varepsilon_{r\text{glass}} - 1\right)\frac{K(k)K(k_2')}{K(k')K(k_2)} \\ &+ \frac{1}{2}\left(\varepsilon_{r\text{BCB}}^{\text{below}} - \varepsilon_{r\text{glass}}\right)\frac{K(k)K(k_3')}{K(k')K(k_3)} \end{aligned} \quad (10)$$

where

$$k_i = \sqrt{1 - \frac{\sinh^2(\pi x_a/2h_i)}{\sinh^2(\pi x_b/2h_i)}}, \qquad i = 1,2,3; \quad k_i' = \sqrt{1-k_i^2}.$$

Using the effective relative permittivity calculated in this way, the capacitive coupling between coplanar metal strips (in the concentric ring configuration) embedded in the multilayer structure may be determined. This allows the calculation of the different capacitances of the lumped-element model.

1) Capacitances to Ground: The calculation of the different elements of the spiral inductor model starts from a concentric circle approximation of the spiral. This means that, in the first instance, the spiral is considered to be symmetrical. This leads to identical capacitances to ground C_1 and C_2, resembled in two new capacitances called C_{12}. Knowing C_0 from (9) and ε_{eff} from (10) yields $C = C_0\varepsilon_{\text{eff}}$ (F/m) using (8) as the real capacitance per unit length between two metal strips. For the actual calculation, we assume the two strips to have the largest width of the following two options: firstly, a strip that represents the part of the spiral that couples to the ground plane, having a width equal to half of the outer radius of the spiral and, secondly, the coplanar ground plane part being typical 300-μm wide. Finally, the model capacitances to ground may be calculated as $C_{12} = C \cdot P_g$, with P_g being the circular perimeter in the center of the gap between outer spiral turn and coplanar ground plane.

2) Inter-Turn Capacitances: The capacitive coupling between the turns, modeled by C_3, is determined similarly as C_{12}, but now the width of the strips for the superposition of partial capacitances is the width of the spiraling conductors. The actual model value is obtained by multiplying the value per unit length by P_c, being half of the total sum of all circular perimeters on the center line of the spiral turns. This yields $C_3 = C \cdot P_c$.

3) Corrections for Planarization Effects: Ideally, the spin-coated thin-film BCB dielectric covers the underlying metal strips such that the top surface remains perfectly flat. This means that the degree of planarization (DOP) of the dielectric is 100% and the dielectric thickness on top and in between each strip is always the same. In practice, the DOP will not be 100%, resulting in a varying thickness of the BCB dielectric on top and in between coplanar metal strips. With a Dektak profile meter, the surface profile on top of the embedded spiral inductors was registered. A typical profile is shown in Fig. 6. Referring to Fig. 7,

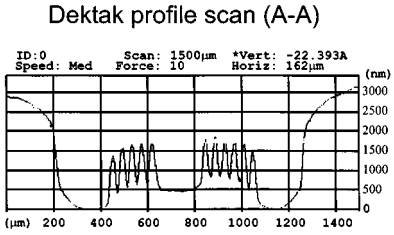

(a)

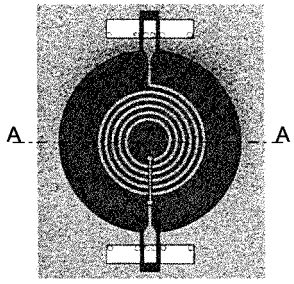

(b)

Fig. 6. Typical profile scan of the top surface above an embedded spiral inductor showing the planarization effect of the BCB dielectric. In this example the inductor has 5.5 turns of 20-μm width and 20-μm gap. The inner gap as well as the spacing to the coplanar ground plane are 200-μm wide.

the DOP over a gap in a large metal plane or over a single metal strip is defined as

$$\text{gap:} \quad \text{DOP}(\%) = 100\left(1 - \frac{t_d}{t_m}\right) \tag{11a}$$

$$\text{strip:} \quad \text{DOP}(\%) = 100\left(1 - \frac{t_r}{t_m}\right). \tag{11b}$$

Recast in a common equation for both cases using the effective dielectric thickness t_{eff} in the gap or on the strip, the definition becomes

$$\text{DOP}(\%) = 100\left(1 - \frac{t_m \pm (t_0 - t_{\text{eff}})}{t_m}\right) \tag{12}$$

with $+$ for a gap and $-$ for a strip.

The planarization effect is, of course, dependent on the feature sizes of the strips and gaps and on the type and thickness of the dielectric. Tests have been carried out to estimate the DOP above strips and gaps with different dimensions [33]. The variation of the DOP in relation with the feature size is displayed in Fig. 8. With this information and knowing the dimensions of the spiral inductors, the actual dielectric thickness may be determined. For gaps, the correction factor to do this is

$$\text{DOP}_{\text{corr}} = -6.82 \cdot 10^{-5} F^3 + 0.01315 F^2 - 1.01117 F + 87.6533 \tag{13}$$

with F being the feature size in micrometers.

For the spiral inductor model presented in this paper, the planarization mainly influences the determination of the parasitic capacitances. Therefore, the correction factor given in (13) has to be included in the calculation of the effective dielectric constants using (10), such that the effective dielectric thickness is taken into account.

C. Resistance

Several formulas for the resistive losses in metal strips may be used for the calculation of the resistance element in the spiral inductor model. The best match with experiments were obtained using the formulas by Owyang and Wu [34] (later adapted and corrected in [35] and [36]), which are specifically for coplanar topologies. The corrected formula from [35] was used in this study (in decibels per unit length)

$$\alpha_c = \frac{8.68 \cdot R_s \sqrt{\varepsilon_{r\_\text{eff}}}}{480\pi d \cdot K(k) \cdot K(k') \cdot (1 - (w/d)^2)} \times \left(\frac{2d}{w}\left\{\pi + \ln\left(\frac{4\pi w(1-(w/d))}{t(1+(w/d))}\right)\right\} + 2\left\{\pi + \ln\left(\frac{4\pi d(1-(w/d))}{t(1+(w/d))}\right)\right\}\right) \tag{14}$$

with $R_s = \sqrt{\pi f \rho \mu_0 \mu_r}$ being the real part of the specific internal surface impedance, f being the frequency of operation, ρ being the resistivity of the conductor metal, $\varepsilon_{r\_\text{eff}}$ being the effective relative permittivity in the structure, t being the conductor thickness, w being the width of the conductor, d being the conductor with plus twice the spacing, and $k = w/d$, $k' = \sqrt{1-k^2}$, and $K(\cdot)$ being the complete elliptical integrals of the first order. From the conductive loss parameter α_c, the value of the series resistance R may be easily obtained.

V. Model Verification by Measurements

In order to verify the analytical spiral inductor model presented in the previous sections, an extensive comparison between measurements and simulation results of all realized spiral inductors was carried out.

A comparison between network analyzer measurement results and simulations results using the proposed model of three exemplary and typical spirals is shown in Fig. 9(a) and (b). This figure shows a good match for the insertion loss and return loss up to the first resonance frequency of each of the inductors. The displayed three inductors are representative results for the typical geometrical range of interest (see Table I). In Fig. 9(c), the same comparison between measurements and model simulations is made for the inductance value L of all inductors of Table I. Here, a good match is observed as well. Only close to the first resonance frequency, a small deviation may be observed for some inductors.

Further comparisons of the maximum of the Q factor $Q\max$ and the frequency of this maximum $fQ\max$ for the inductors of the typical inductor set of Table I are shown in Fig. 10. It is clear that the proposed model predicts the quality behavior of the inductor accurately. This is in spite of the fact that $Q\max$ and $fQ\max$ are normally hard to predict since they are severely influenced by a mix of parasitic effects occurring in the spiral. In our case, only for small inductance values, the $Q\max$ and $fQ\max$ are slightly overestimated, but quite accurate for the others. The overestimation in case of the small values is because slight differences in calculation of the small parasitic effect may already result in more significant changes of the Q factor behavior.

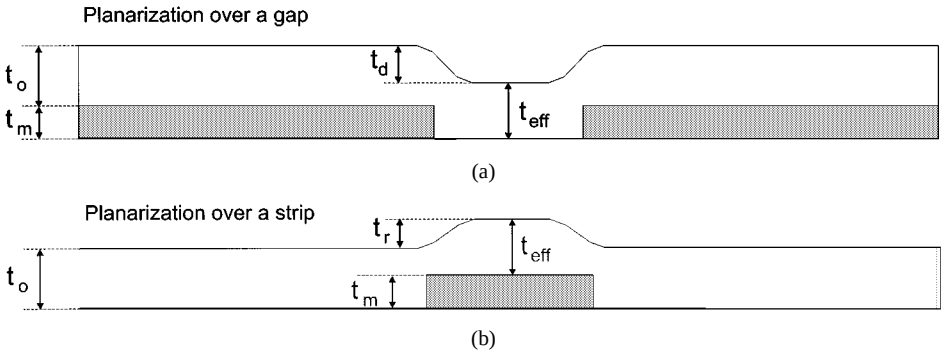

Fig. 7. Schematic drawing indicating the parameters involved in the calculation of the DOP over gaps and strips.

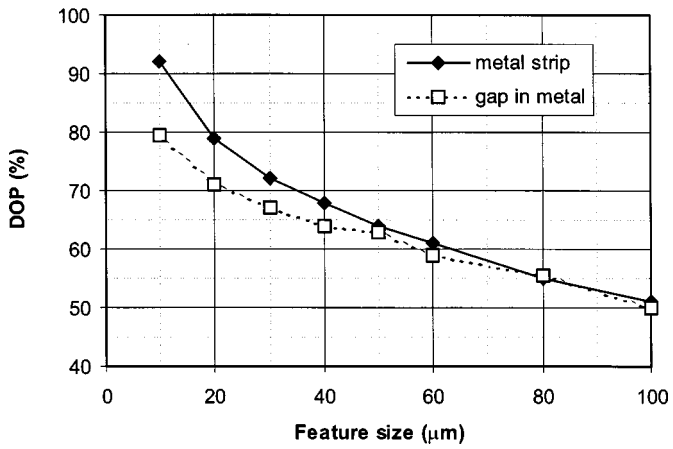

Fig. 8. Variation of the DOP of a photosensitive BCB dielectric on top of metal strips or gaps in the metal with different sizes [33].

The typical calculation time for one spiral inductor with 3.5 turns is a few seconds on an HP J5000 station.

VI. Optimization and Spiral Inductor Design Spaces

The inductance value L of the spiral inductor, together with its Q factor and the frequency of application f determine the actual usefulness of the component in practical circuits. One wants to have that specific spiral inductor that provides the maximum Q for a given L at the appropriate frequency f. A graphical representation of these three parameters is shown in Fig. 11 for both the measured, as well as the analytically calculated, values of the inductors listed in Table I. These two so-called spiral inductor designs spaces agree very well, indicating that the presented model predicts the spiral inductor frequency behavior accurately.

In a next step, the spiral inductor model may be used to calculate the inductor characteristics for any possible inductor geometry, enabling a search for the optimum inductor geometry that provides the maximum Q for the given L and frequency range. In other words, we may build an inductor design space containing all optimum inductors. Furthermore, area restriction may be inserted in the optimization procedure, yielding the creation of design spaces with "good-enough Q" inductors for a given inductance range, frequency range, and area. The use of such optimized inductor design spaces may be a powerful tool for fast and accurate design of high-performance RF and microwave front-end systems.

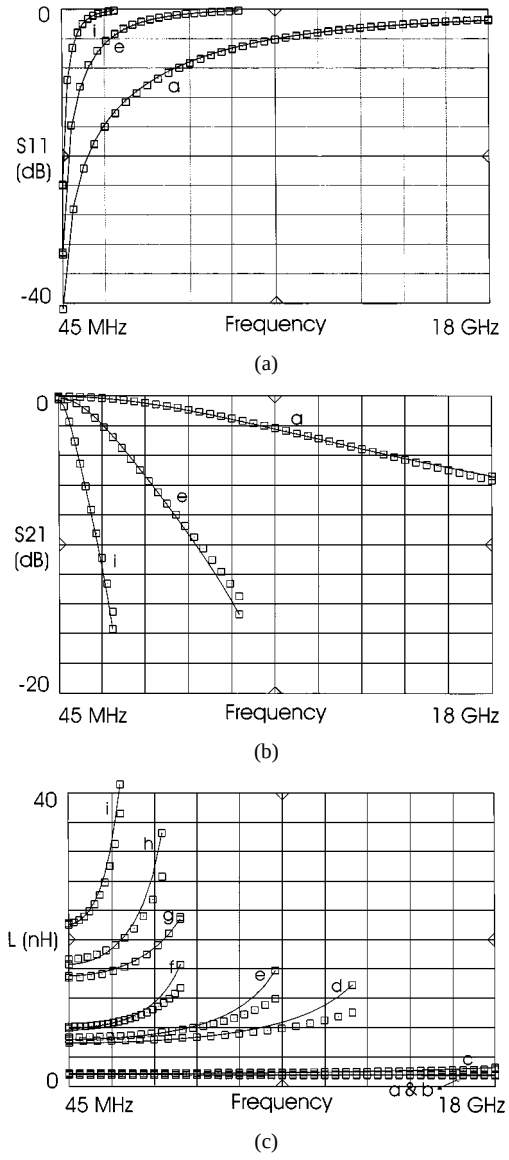

Fig. 9. Comparison of the measured (solid line) and calculated model (dotted line) (a) return loss and (b) insertion loss for three typical inductors versus frequency. The three inductors (see also Table I for labels a, e, and i) cover a wide geometrical range. (c) Comparison of the measured (solid line) and calculated model (dotted line) inductance value versus frequency for the inductors of Table I.

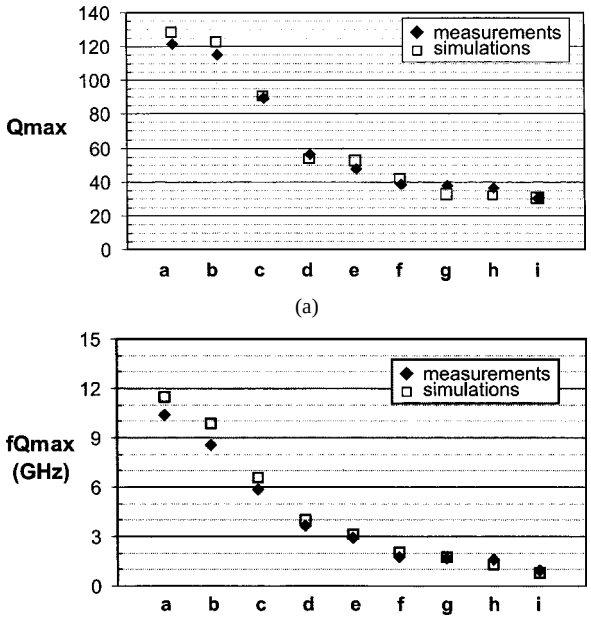

Fig. 10. (a) Comparison of measured and with the proposed model calculated maximum Q factor for the set of typical spiral inductors listed inTable I (labels a–i). (b) Comparison of measured and with the proposed model calculated frequency of the maximum Q factor for the set of typical spiral inductors listed in Table I (labels a–i).

VII. Applications

Wireless applications such as digital enhanced cordless telephony (DECT) at 1.8 GHz, universal mobile telecommunication system (UMTS) at 2.2 GHz, Bluetooth at 2.4 GHz, wireless local area network (WLAN) at 5.2 GHz are emerging rapidly. The transmit–receive front-ends of all these applications contain many passive components. Integrating them into a common multilayer carrier substrate and mounting the active devices onto this substrate using flip chip or wire bonding increases the packaging density tremendously. Moreover, since integrated passives have reduced parasitics and less solder joints compared to surface-mount components, respectively, the electrical performances and reliability of the systems are increased. The integration of high-Q spiral inductors may especially play a major role in this evolution.

In the following sections, a number of examples of circuits and front-end subsystems fully integrated in thin-film multilayer MCM-D technology are introduced. The basis of all the presented examples is the need for predictable high-Q inductors.

A. 5.2-GHz Lumped Rat Race

A lumped-element rat-race circuit needs to have very reproducible and high-Q components to maintain good balance and low insertion loss. Starting from the basic equivalent circuit and the well-known design equations for such a coupler [37], six capacitors of 866 fF and six inductors of 2.16 nH (with $Q = 88.5$ at 6 GHz) were needed to realize a 5.2-GHz rat race for application in WLAN front-ends. In Fig. 12, a photograph of the rat-race circuit integrated in the above-described thin-film multilayer MCM-D technology is shown. The simulations (using the presented spiral inductor model) and the vector-network analyzer measurements for the in-phase and antiphase

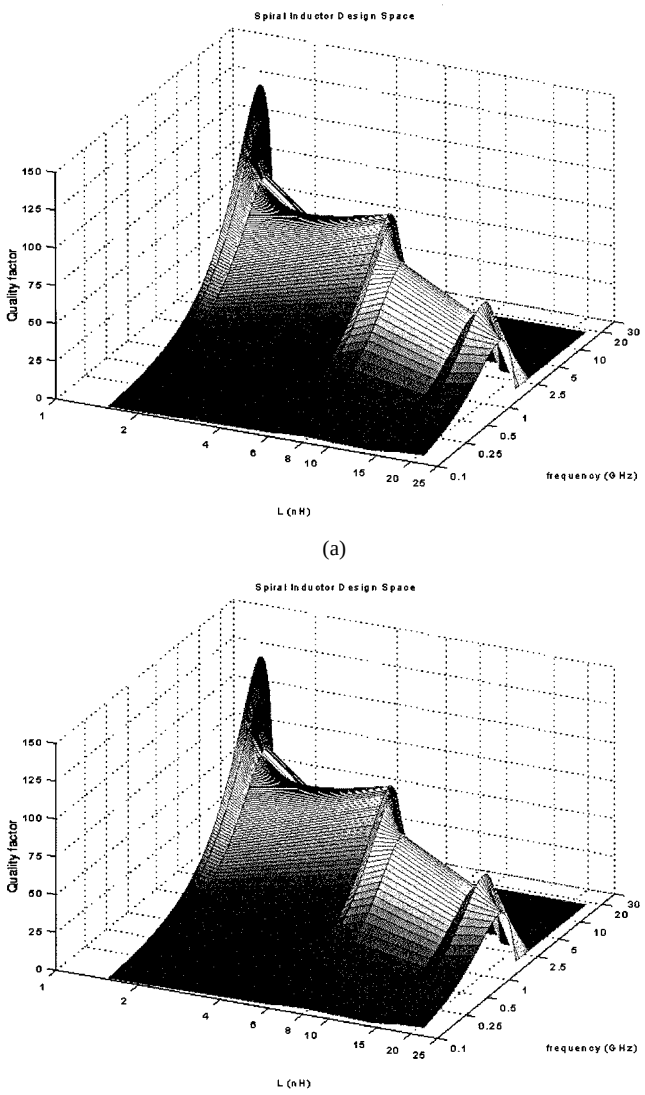

Fig. 11. Comparison between the inductor design space of the spirals listed in Table I, (a) extracted from measurements and (b) calculated using the presented model.

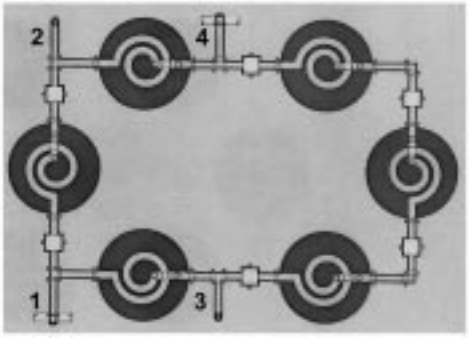

Fig. 12. Photograph of a 5.2-GHz rat-race circuit for WLAN applications fully integrated in thin-film multilayer MCM-D technology. Total size: 4.3 mm × 6.3 mm.

branch, as well as the phase balance and imbalance, are compared in Fig. 13. Low insertion loss (0.24-dB maximum) and good agreement between measurements and simulations is observed, especially in the desired coupling range. Only the phase

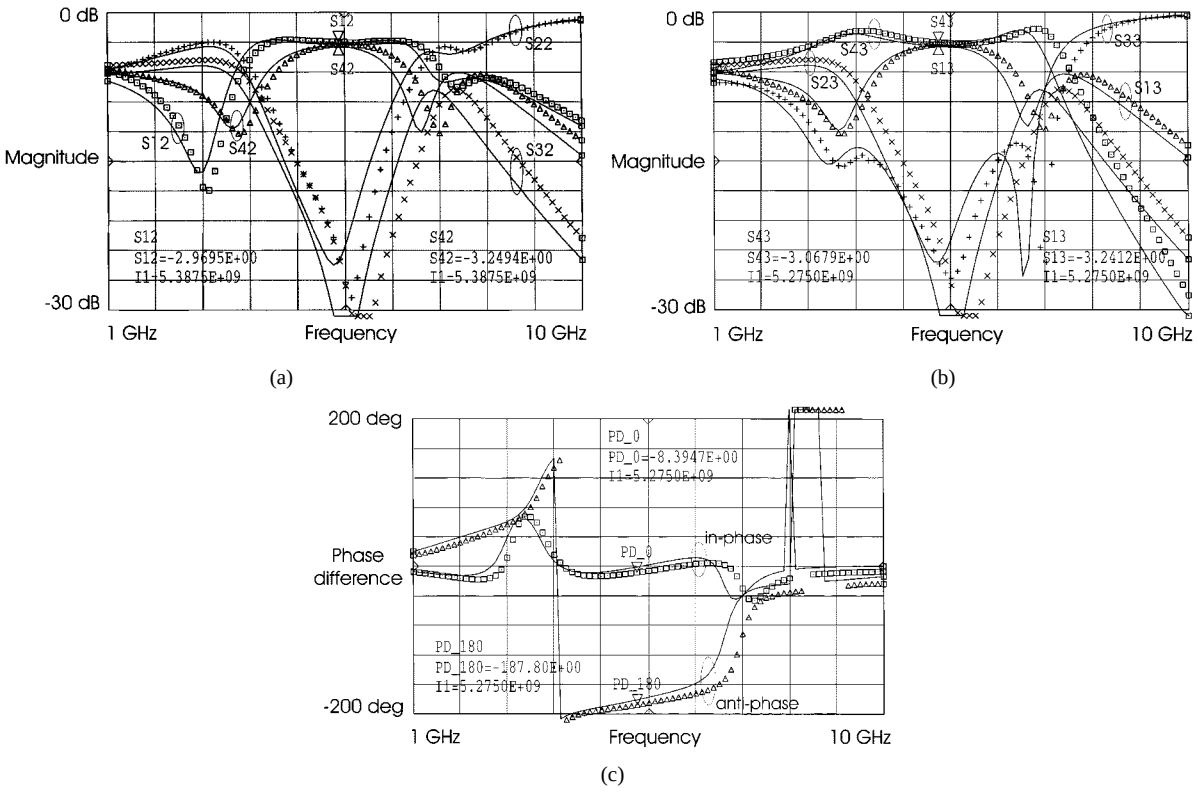

Fig. 13. Comparison between network-analyzer measurements and simulations of the 5.2-GHz rat race of Fig. 12. Solid lines are simulations. (a) Magnitude of in-phase outputs, return loss, and isolation. (b) Magnitude of antiphase outputs, return loss, and isolation. (c) Phase difference for in-phase and antiphase outputs.

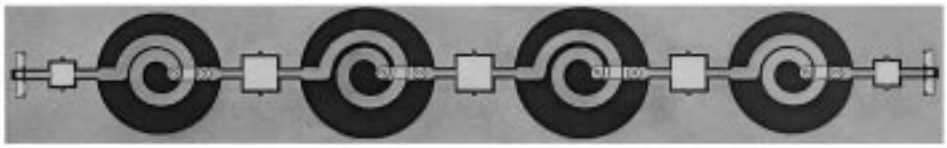

Fig. 14. Photograph of a 5.2-GHz ninth-order low-pass filter for WLAN applications fully integrated in thin-film multilayer MCM-D technology. Total size: 10 mm $\times$ 1.5 mm.

difference deviates a few degrees from 0° and 180° at the center of the band. This is most likely caused by the on-wafer measurement sequence. The four-port circuit was measured using a two-port network analyzer. To do so, the structure was repeated several times, each version having two different ports terminated by an embedded 50-Ω resistor and the two other open for probing. With six different two-port measurements, the circuit could be completely measured.

B. 5.2-GHz Low-Pass Filter

A photograph of a ninth-order low-pass filter consisting of a ladder network of five capacitors to ground and four series inductors is shown in Fig. 14. For a low-pass corner frequency of -1.5 dB at 5.2 GHz, the capacitors range from 422 to 916 fF and the inductors range from 2 to 2.4 nH (with $Q = 82$ at 5 GHz). A comparison between network-analyzer measurements and model simulations for the $S21$ insertion loss and $S11$ returns loss is shown in Fig. 15. The agreement between measurements and model simulations (using the proposed spiral inductor model) is very good for both return loss and insertion loss. Notwithstanding the four spirals in series, the insertion loss remains very low due to the high-Q factor of the inductors.

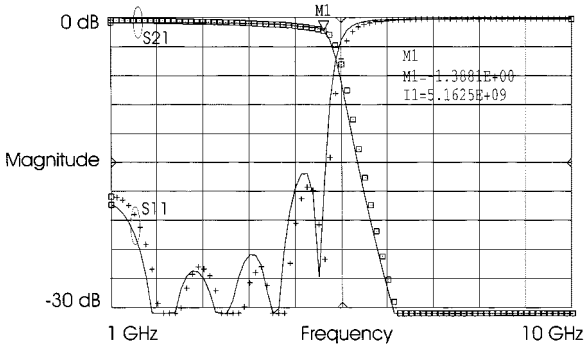

Fig. 15. Comparison between network-analyzer measurement results and simulations (solid lines) of the integrated ninth-order low-pass filter shown in Fig. 14.

C. 3-GHz Integrated Coupled Spirals Balun

Baluns are important elements in front-end systems where they provide conversion from a single unbalanced input to two

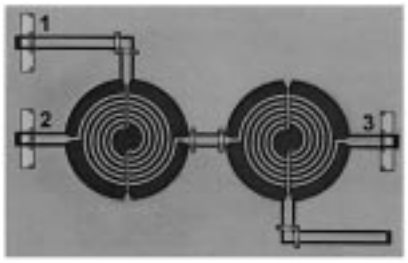

Fig. 16. Photograph of a 3-GHz coupled coil balun fully integrated in thin-film multilayer MCM-D technology. Total size: 3.3 mm × 1.8 mm.

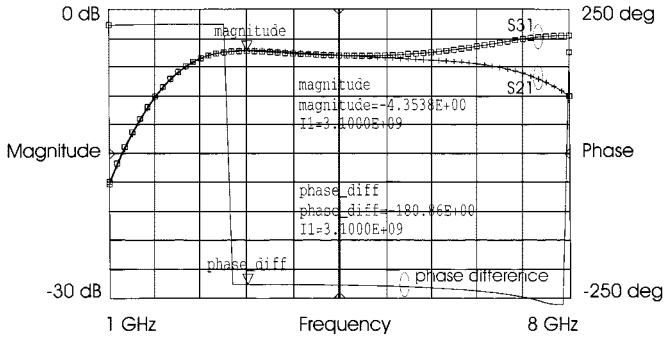

Fig. 17. Measurement results of the nested coupled coil balun of shown in Fig. 16. The measured amplitude balans as well as the 180° phase balans between the two outputs is practically flat in a band from about 3–5 GHz.

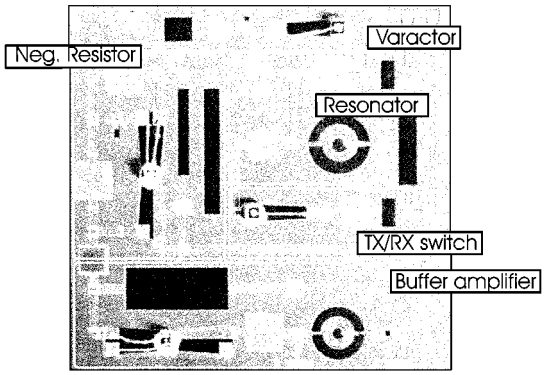

Fig. 18. Photograph of a DECT VCO integrated in thin-film multilayer MCM-D technology. Total size 7.5 mm × 7.5 mm [19].

balanced outputs or vice versa for, e.g., balanced mixers, amplifier stages, or antennas. Traditionally, a Marchand balun type with coupled quarter-wavelength sections is used to realize passive integrated baluns. However, for wireless applications in the 1–6-GHz range, the size of these couplers becomes too large. Here, lumped-element baluns and especially nested spiral inductor baluns become very attractive. In Fig. 16, a photograph of such a nested coupled coil balun at 3 GHz is shown. From the measurement results given in Fig. 17, one can see that the amplitude and phase are in good balance over a broad frequency range from about 3–5 GHz. The insertion loss is around 1.4 dB (with respect to −3 dB), which is acceptable considering the coupling through large nested spiral inductors, and better than the example shown in [22].

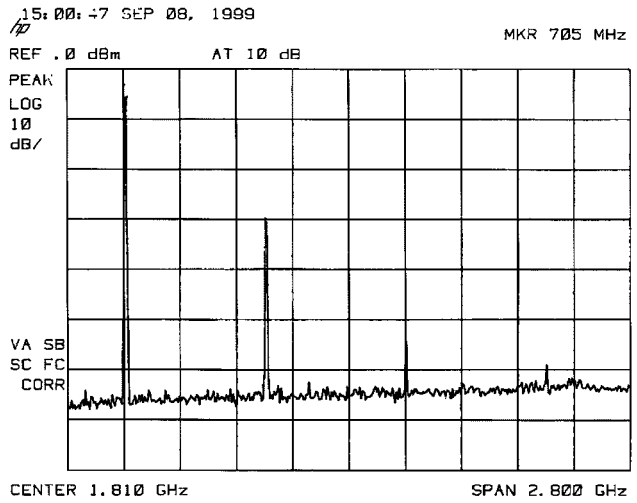

(a)

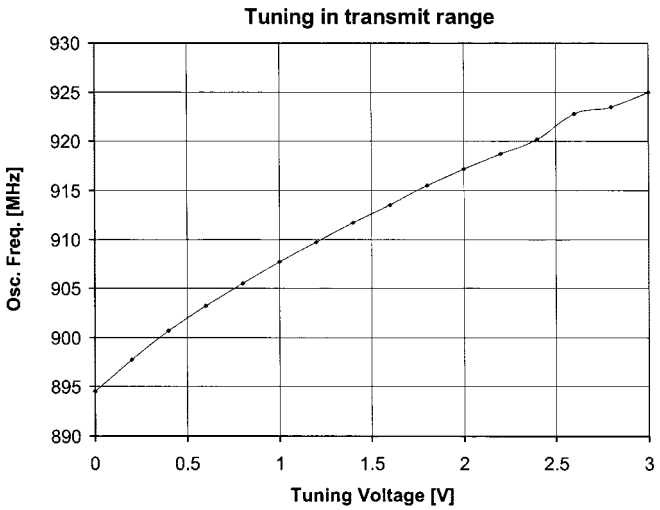

(b)

Fig. 19. Measurement results for the DECT VCO integrated in MCM-D shown in Fig. 18 (a) Free-running output power spectrum. (b) Measured transmit tuning range of the VCO for the full 3-V voltage swing.

D. DECT Voltage-Controlled Oscillator

A photograph of a voltage-controlled oscillator (VCO) module for a DECT application integrated in thin-film multilayer MCM-D is shown in Fig. 18. All 28 passive component (resistors, capacitors, and inductors) are integrated into and the four active devices are wire bonded onto the interconnection substrate. In this way, a miniature system of 7.5 mm × 7.5 mm is realized [19], which is four times smaller than the presently used printed-circuit-board version. Wire bonding had to be used because the bare die active devices had contacts at both the top and bottom sides. The VCO circuit operates at half of the DECT operational frequency, as a frequency doubler up to 1890 MHz is available in the accompanying RF chip. The measured performance characteristics of the VCO are −5-dBm output power, 894.5–925 MHz (transmit) and 826.5–845.3 MHz (receive) tuning range, 10.2 MHz/V (transmit) and 6.1 MHz/V (receive) tuning sensitivity, −117.9-dBc/Hz phase noise at 1.72 MHz from the carrier frequency (limited by the dynamic range of the measurement equipment), and −109.7-dBc/Hz phase noise

at 100 kHz from the carrier frequency. The phase noise of −117.9 dBc/Hz at 1.72 MHz from the carrier frequency is 14.9 dB better than the DECT specifications. This achievement may be dedicated to the excellent high-Q integrated spiral inductors. Finally, in Fig. 19, the free running output power spectrum and the measured transmit tuning range are shown.

VIII. Conclusions

High-Q spiral inductors integrated in a thin-film multilayer or MCM-D technology for RF and microwave frequencies have been demonstrated in this paper. Their inductance value may go above 100, which is much more than what is possible for inductors on silicon. These high-Q inductors have a big potential for low-power, low-noise, and high-performance portable applications. Moreover, by combining active circuits on a chip together with high-Q passives integrated in the MCM-D substrate, further RF system miniaturization and performance increase is possible.

The presented spiral inductor model allows an accurate prediction of the component's inductance value, Q factor, and frequency behavior, starting from the geometrical parameters. This is very important in the circuit design phase in order to have a "first-time-right" realization of the fully integrated inductors. Moreover, the short model calculation time allows the optimization of the geometry of the inductor. In this way, it is possible to determine the optimum spiral inductor for a given inductance value and frequency range. The various examples at the end of this paper indicate the usefulness of the high-Q inductors for wireless telecommunication applications in terms of miniaturization and performance enhancement.

References

[1] J. Rector, J. Dougherty, V. Brown, J. Galvagni, and J. Prymak, "Integrated and integral passive components: A technology roadmap," in *Proc. 47th Electron. Comp. Technol. Conf.*, 1997, pp. 713–723.

[2] H. Kapadia, H. Cole, R. Saia, and K. Durocher, "Evaluating the need for integrated passive substrates," *Adv. Microelectron.*, vol. 26, no. 1, pp. 12–15, 1999.

[3] W. B. Baringer and R. W. Brodersen, "MCM's for portable applications," in *Proc. IEEE Multichip Module Conf.*, Santa Cruz, CA, 1993, pp. 1–5.

[4] T.-H. Lin, H. Sanchez, R. Rofougaran, and W. J. Kaizer, "CMOS front end components for micropower RF wireless systems," in *Proc. Int. Low-Power Electron. Design Symp.*, Monterey, CA, 1998, pp. 11–15.

[5] J. R. Long and M. A. Copeland, "Modeling, characterization and design of monolithic inductors for silicon RFIC's," in *Proc. Custom Integrated Circuits Conf.*, 1996, pp. 185–188.

[6] J. N. Burghartz, M. Soyer, K. A. Jenkins, and M. D. Hulvey, "High-Q inductors in standard silicon interconnect technology and its application to an integrated RF power amplifier," in *Proc. Int. Electron Devices Meeting*, Washington, DC, 1995, pp. 1015–1018.

[7] J. N. Burghartz, D. C. Edelstein, K. A. Jenkins, and Y. H. Kwark, "Spiral inductors and transmission lines in silicon technology using copper-damascene interconnects and low-loss substrates," *IEEE Trans. Microwave Theory Tech.*, vol. 45, pp. 1961–1968, Oct. 1997.

[8] D. C. Edelstein and J. N. Burghartz, "Spiral and solenoidal inductor structures pm silicon using Cu–damascene interconnects," in *Proc. Int. Interconnect Technol. Conf.*, San Francisco, CA, 1998, pp. 18–20.

[9] V. Malba, D. Young, J. J. Ou, A. F. Bernhardt, and B. E. Boser, "High-performance RF coil inductors on silicon," in *Proc. Electron. Comp., Technol. Conf.*, Seattle, WA, 1998, pp. 252–255.

[10] T. Shimoto, K. Matsui, and K. Utsumi, "Cu/photosensitive–BCB thin film multilayer technology for high performance multichip modules," *IEEE Trans. Comp., Packag., Manufact. Technol. A*, vol. 18, pp. 11–15, Feb. 1995.

[11] C. Truzzi, E. Beyne, and E. Ringoot, "Performance analysis of a 10-Gbit/s digital switch on MCM," in *Proc. IEEE Int. Innovative Syst. Silicon Conf.*, Austin, TX, 1996, pp. 238–248.

[12] ——, "MCM-D for high-speed digital applications—Electrical modeling and performance evaluation," in *Proc. Int. Multichip Modules Conf.*, Denver, CO, 1997, pp. 29–34.

[13] N. Yamanaka, T. Kawamura, K. Kaizu, and A. Harada, "Advanced ATM switching system hardware technology using MCM-D, stacking RAM micro-processor module," in *Proc. Electron. Comp., Technol. Conf.*, 1998, pp. 884–888.

[14] Y. Lee, D. E. Chung, S. P. Lee, J. H. Na, C. W. Ju, S.-S. Park, and M. K. Song, "A new 16 × 16 ATM switching multichip module with high performance," in *Proc. Multichip Modules Conf.*, Denver, CO, 1999, pp. 266–269.

[15] R. G. Arnold and D. J. Pedder, "Microwave characterization of microstrip lines and spiral inductors in MCM-D technology," *IEEE Trans. Comp., Hybrids, Manufact. Technol.*, vol. 15, pp. 1038–1045, Dec. 1992.

[16] P. Pieters, S. Brebels, and E. Beyne, "Integration of passive components for microwave filters in MCM-D," in *Proc. Int. Multichip Modules Conf.*, Denver, CO, 1997, pp. 357–362.

[17] M. de Samber, N. Puslford, M. van Delden, and R. Milsom, "Low-complexity MCM-D technology with integrated passives for high frequency applications," in *Proc. Int. Multichip Modules Conf.*, Denver, CO, 1998, pp. 285–290.

[18] D. C. Benson, Y. Xuan, J. He, C.-M. Lin, C. R. Hodges, E. A. Logan, T. M. Schaefer, and B. K. Gilbert, "Integrated passive components for RF applications," in *Proc. Wireless Commun. Conf.*, Boulder, CO, 1997, pp. 175–180.

[19] K. Vaesen, P. Pieters, G. Carchon, W. De Raedt, and E. Beyne, "Integrated passives for a DECT VCO," in *Proc. Int. High-Density Interconnect Syst. Packag. Conf.*, Denver, CO, 2000, pp. 537–541.

[20] P. Pieters, S. Brebels, E. Beyne, and R. P. Mertens, "Generalized analysis of coupled lines in multilayer microwave MCM-D technology—Application: Integrated coplanar Lange couplers," *IEEE Trans. Microwave Theory Tech.*, vol. 47, pp. 1863–1872, Sept. 1999.

[21] P. Pieters, S. Brebels, W. De Raedt, E. Beyne, and R. P. Mertens, "Distributed microwave MCM-D circuits for X- and K-band applications," *Int. J. Microcircuits Electron. Packag.*, vol. 22, no. 3, pp. 280–287, 1999.

[22] Y. J. Yoon, Y. Lu, R. C. Frye, M. Y. Lau, P. R. Smith, L. Ahlquist, and D. P. Kossives, "Design and characterization of multilayer spiral transmission-line baluns," *IEEE Trans. Microwave Theory Tech.*, vol. 47, pp. 1841–1847, Sept. 1999.

[23] E. A. Soliman, S. Brebels, E. Beyne, P. Delmotte, and G. A. E. Vandenbosch, "Brick-wall antenna in multilayer thin-film technology," *Microwave Opt. Technol. Lett.*, vol. 19, pp. 360–365, Dec. 1998.

[24] ——, "Circularly polarized aperture antenna fed by CPW and built in MCM-D technology," *Electron. Lett.*, vol. 35, pp. 250–251, Feb. 1999.

[25] E. A. Soliman, S. Brebels, G. A. E. Vandenbosch, and E. Beyne, "Antenna arrays in MCM-D technology fed by coplanar CPW networks," *IEEE Trans. Microwave Theory Tech.*, to be published.

[26] C. C. Faulkner and S. M. Jones, "An MCM based Hiperlan radio subsystem," in *Proc. IEE RF Microwave Circuits Commercial Wireless Applicat. Colloq.*, London, U.K., 1997, pp. P.9/1–P.9/7.

[27] K. Vaesen, S. Brebels, W. De Raedt, E. Beyne, A. Naem, and R. Kohlmann, "Realization of a DECT VCO circuit with MCM-D technology," in *Pro. Int. Microelectron. Conf.*, 1999, pp. 141–144.

[28] P. Pieters, S. Brebels, G. Carchon, K. Vaesen, W. De Raedt, E. Beyne, and R. P. Mertens, "On the dielectric material properties for thin film integrated RF and microwave applications," *Adv. Microelectron.*, vol. 26, no. 5, pp. 19–23, 1999.

[29] S. Donnay, P. Pieters, K. Vaesen, W. Diels, P. Wambacq, W. De Raedt, E. Beyne, M. Engels, and I. Bolsens, "Chip-package codesign of a low-power 5-GHz RF front end," *Proc. IEEE*, vol. 88, pp. 1583–1597, Oct. 2000.

[30] H. Pranjoto and D. D. Denton, "Moisture uptake of bisbenzocyclobutene (BCB) films for electronic packaging applications," in *Proc. Electron. Packag. Mater. Sci. Symp.*, Boston, MA, 1990, pp. 295–302.

[31] S. F. Mahmoud and E. Beyne, "Inductance and quality-factor evaluation of planar lumped inductors in a multilayer configuration," *IEEE Trans. Microwave Theory Tech.*, vol. 45, pp. 918–923, June 1997.

[32] E. Chen and S. Y. Chou, "Characteristics of coplanar transmission lines on multilayer substrates: Modeling and experiments," *IEEE Trans. Microwave Theory Tech.*, vol. 45, pp. 939–945, June 1997.

[33] E. Beyne, R. Van Hoof, and A. C. Aachen, "The use of BCB and photo-BCB dielectrics in MCM-D for high-speed digital and microwave applications," in *Proc. Int. Multichip Modules Conf.*, Denver, CO, 1995, pp. 513–518.
[34] G. H. Owyang and T. T. Wu, "The approximate parameters of slot lines and their complement," *IRE Trans. Antennas Propagat.*, vol. AP-6, p. 49, Jan. 1958.
[35] R. K. Hoffmann, *Handbook of Microwave Integrated Circuits*. Norwood, MA: Artech House, 1987, p. 357.
[36] R. Royal, Ed., *Monolithic Microwave Integrated Circuits: Technology and Design*. Norwood, MA: Artech House, 1989, p. 375.
[37] I. D. Robertson, "MMIC design," in *IEE Circuits and Systems Series*, ser. 7. London, U.K.: IEE, 1995.

Philip Pieters (S'93) received the Industrial Engineering degree and the M.S. degree in electrical engineering from the Catholic University of Leuven, Leuven, Belgium, in 1991 and 1994, respectively.

In 1994, he joined the High Density Interconnection and Packaging Group, Interuniversity Microelectronics Centre (IMEC), Leuven, Belgium, where he initiated research on integrated passives in multilayer thin-film MCM-D technology. Since April 2000, he has been with the Technology Development Department, CS2 (a semiconductor assembly and test foundry), Zaventem, Belgium, where he is responsible for high-frequency development projects.

Kristof Vaesen received the Industrial Engineering degree from the Karel de Grote Hogeschool (KdG), Antwerp, Belgium, in 1996, and the M.S. degree in electrical engineering from the Catholic University of Leuven, Leuven, Belgium, in 1998.

He then joined the High Density Interconnect and Systems Packaging Group, Interuniversity Microelectronics Centre (IMEC), Leuven, Belgium, where since then, his main research activities have been focused toward the single-package integration of RF front-ends and the design of RF building blocks in RF MCM-D technology.

Steven Brebels (S'92) was born on October 25, 1971, in Neerpelt, Belgium. He received the M.S. degree in electrical engineering from the Catholic University of Leuven, Leuven, Belgium, in 1994, and is currently working toward the Ph.D. degree at the Interuniversity Microelectronics Centre (IMEC), Leuven, Belgium.

His research within the High Density Interconnect and Packaging Group, IMEC, is directed to integrated microwave circuits and antennas in MCM-D. His research interests include microwave and millimeter-wave ICs and active integrated antennas.

Samir F. Mahmoud (S'69–M'73–SM'83) received the Electronic Engineering degree from Cairo University, Cairo, Egypt, in 1964, and the M.Sc and Ph.D. degrees in electrical engineering from Queen's University, Kingston, ON, Canada in 1970 and 1973, respectively.

During the 1973–1974 academic year, he was a Visiting Research Fellow at the Cooperative Institute for Research in Environmental Sciences (CIRES), Boulder, CO. He spent two sabbatical years (1980–1982) between Queen Mary College, London, U.K., and British Aerospace, Stevenage, U.K., where he was involved in research on design of feeds for satellite antennas. From 1964 to 1995, he was with the Electronic Engineering Department, Cairo University, where since 1985, he had been a Professor. He is currently a Professor in the Electrical and Computer Engineering Department, Kuwait University, Kuwait. His research activities have been in the areas of geophysical applications of electromagnetic waves, communication in mine tunnels, satellite antennas, microwave components, and microwave interaction with chiral materials. He authored *Electromagnetic Waveguides: Theory and Applications* (IEE Electromag. Ser.) (London, U.K.: IEEE Press, 1991).

Walter De Raedt received the M.S. degree in electrical engineering from the Catholic University of Leuven, Leuven, Belgium, in 1981.

He subsequently joined the Electronics, Systems, Automation, and Technology (ESAT) Laboratory, where he was a Research Assistant involved with direct write electron beam technology. Since 1984, he has been with the Interuniversity Microelectronics Centre (IMEC), Leuven, Belgium, where he has been involved with research on MICs and submicrometer technologies for advanced high electron-mobility transistor (HEMT) devices. Since 1997, he has been with the High Density Interconnection and Packaging Group, IMEC, where he coordinates projects on integrated passives and interconnections for RF front-end systems.

Eric Beyne was born on May 26, 1960, in Tienen, Belgium. He received the Electrical Engineering degree and Ph.D. degree in applied sciences from the Catholic University of Leuven, Leuven, Belgium, in 1983 and 1990, respectively.

From 1983 to 1985, he was a Research Assistant at the Catholic University of Leuven. In 1986, he joined the Interuniversity Microelectronics Centre (IMEC), Leuven, Belgium, where he was involved with research on the interconnection of high-frequency digital circuits. He is currently the Head of the High Density Interconnection and Packaging Group, IMEC.

Dr. Beyne is the secretary of the International Microelectronics and Packaging Society (IMAPS) Benelux Committee.

Robert P. Mertens (M'80-SM'86-F'95) received the Ph.D. degree from the Catholic University of Leuven, Leuven, Belgium, in 1972.

In 1973, he was a Visiting Scientist at the University of Florida. After his return to Belgium in 1974, he became a Senior Research Associate at the National Foundation for Scientific Research of Belgium. In 1984, he joined the Interuniversity Microelectronics Centre (IMEC), Leuven, Belgium, where he is currently the Senior Vice President for Micro-Systems, Components, and Packaging. His activities also include research on photovoltaics and solid-state sensors. Since 1984, he has also been a Professor at the Catholic University of Leuven, where he teaches courses on devices and technology of electronic systems.